

Structural Basis for Calcium Sensing by GCaMP2

Qi Wang,¹ Bo Shui,² Michael I. Kotlikoff,² and Holger Sondermann^{1,*}

¹Department of Molecular Medicine

²Department of Biomedical Sciences

College of Veterinary Medicine, Cornell University, Ithaca, NY 14853, USA

*Correspondence: hs293@cornell.edu

DOI 10.1016/j.str.2008.10.008

SUMMARY

Genetically encoded Ca^{2+} indicators are important tools that enable the measurement of Ca^{2+} dynamics in a physiologically relevant context. GCaMP2, one of the most robust indicators, is a circularly permuted EGFP (cpEGFP)/M13/calmodulin (CaM) fusion protein that has been successfully used for studying Ca^{2+} fluxes in vivo in the heart and vasculature of transgenic mice. Here we describe crystal structures of bright and dim states of GCaMP2 that reveal a sophisticated molecular mechanism for Ca^{2+} sensing. In the bright state, CaM stabilizes the fluorophore in an ionized state similar to that observed in EGFP. Mutational analysis confirmed critical interactions between the fluorophore and elements of the fused peptides. Solution scattering studies indicate that the Ca^{2+} -free form of GCaMP2 is a compact, predocked state, suggesting a molecular basis for the relatively rapid signaling kinetics reported for this indicator. These studies provide a structural basis for the rational design of improved Ca^{2+} -sensitive probes.

INTRODUCTION

Genetically encoded Ca^{2+} indicators (GECIs) enable the monitoring of intracellular signaling events in defined cell lineages within complex multicellular tissues, without disrupting cell-cell contacts or permeabilizing cell membranes (Ledoux et al., 2008; Mao et al., 2008; Miyawaki et al., 1997, 1999; Nausch et al., 2008; Roell et al., 2007; Tallini et al., 2006, 2007). Several distinct strategies have been employed to achieve the goals of a bright, fast, high signal-to-noise indicator that functions under in vivo conditions, including the modification of the green fluorescent protein (GFP) family from *Aequorea victoria* (Kotlikoff, 2007; Mank and Griesbeck, 2008; Mao et al., 2008; Palmer and Tsien, 2006; Pologruto et al., 2004; Reiff et al., 2005).

Intact GFP has a cage-like structure with 11 β sheets forming a barrel around a helix containing the fluorescent moiety (Brecj et al., 1997; Ormo et al., 1996; Yang et al., 1996). Protected from solvent access and coordinated by a number of water molecules and polar side chains contributed by the cage, three consecutive residues in the central helix (Ser-Tyr-Gly) undergo posttranslational cyclization to form the fluorophore (Tsien, 1998). Spectroscopic and structural studies have illuminated the molecular mechanism underlying GFP fluorescence (Tsien, 1998). Wild-type GFP (class 1 GFP) has a major excitation peak at a wave-

length of 395 nm and a minor peak at 475 nm, resulting from a protonated and a deprotonated fluorophore, respectively, with distinct emission properties (503 nm versus 508 nm). Neutralizing effects of close-by residues maintain the fluorophore in its protonated state. The fluorophore is subject to reversible ionization facilitated by a surrounding hydrogen bond network involving interactions with the cage wall. Mutation of Ser-65 of the chromophore to threonine yielded an enhanced green fluorescent protein (EGFP) with a deprotonated fluorophore and a single excitation peak at 489 nm (GFP-S65T; class 2 GFP) (Ormo et al., 1996).

GFP is amenable to large structural rearrangements without disrupting its basic fluorescent properties, including circular permutation (Baird et al., 1999). Progressive improvements in sensor performance have been made using a central circularly permuted enhanced green fluorescent protein (cpEGFP) moiety flanked by the M13 helix of myosin light chain and calmodulin (CaM) at the N and C terminus, respectively (GCaMP2 or pericam; Figure 1A) (Nagai et al., 2001, 2004; Nakai et al., 2001; Souslova et al., 2007; Tallini et al., 2007). These molecules exploit Ca^{2+} -dependent intramolecular conformational changes to control the efficiency of fluorophore function. However, the structural basis for Ca^{2+} -dependent changes in fluorescence is not understood, constraining the rational design and optimization of these proteins.

The construction and optimization of novel Ca^{2+} indicators or other molecular sensors based on this strategy currently require extensive random mutagenesis and screening because of our limited understanding of the working mechanism of the current molecules. Here, we determined structures of GCaMP2 in multiple states revealing a surprisingly sophisticated network of interactions between the cpEGFP and CaM moieties that are responsible for the high functionality of this Ca^{2+} probe. These studies will guide the structurally motivated improvement of current molecules and the design of novel indicators.

RESULTS AND DISCUSSION

Crystal Structures of cpEGFP and GCaMP2• Ca^{2+}

Initial studies were carried out with the original GCaMP2 protein containing the N-terminal hexahistidine tag and RSET module (Nakai et al., 2001) (Figure 1). Removal of the purification tag and RSET motif yielded crystals of the bright, Ca^{2+} -bound state of GCaMP2. The N-terminal truncations had no effect on basic properties and efficiency of GCaMP2 at room temperature (expression and purification, spectroscopic properties, and Ca^{2+} response; see Figure S1 available online) suggesting that these domains mainly affect the GCaMP2 folded state under in vivo conditions (Tallini et al., 2006). If not indicated otherwise, the

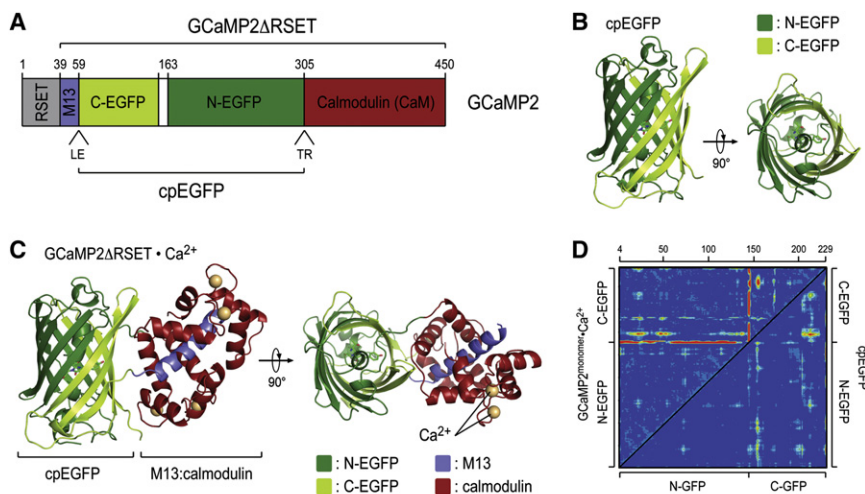


Figure 1. Crystal Structures of GCaMP2•Ca²⁺ and cpEGFP

(A) Domain organization of GCaMP2 and truncated derivatives. A schematic presentation of the GCaMP2 fusion protein is shown. The color scheme introduced here is maintained throughout the article. Residue numbering for circularly permuted EGFP (cpEGFP) and GCaMP2ΔRSET follows the sequence of GCaMP2.

(B) Crystal structure of the isolated cpEGFP moiety. The C-terminal fragment of C-EGFP is colored in light green, and the N-terminal fragment is colored in dark green. Two orthogonal views are shown.

(C) Crystal structure of monomeric GCaMP2ΔRSET in its Ca²⁺-bound state. Crystals were grown in the presence of 1 mM Ca²⁺. Two orthogonal views are shown. The M13 helix is shown in blue, and the calmodulin (CaM) domain is shown in red. The cpEGFP is colored as described in (B).

(D) Comparison of crystal structures of GCaMP2,

cpEGFP, and GFP-S65T. Distance difference matrices based on Cα positions were used to compare the conformation of cpEGFP in isolation (bottom-right triangle) and as part of GCaMP2 (top-left triangle) with the structure of GFP-S65T (PDB code 1EMA; see Supplemental Experimental Procedures). Difference matrices were regularized using a Z-score analysis and color-coded accordingly. Each entry in the matrix depicts the difference in distance between corresponding Cα atoms in the two structures. Distances that show little change are blue. Red entries represent distances that are significantly different in the two structures.

truncated form, GCaMP2ΔRSET, was used in subsequent experiments.

Crystallization trials carried out with native GCaMP2ΔRSET and cpEGFP yielded crystal structures of monomeric GCaMP2ΔRSET•Ca²⁺ and the isolated cpEGFP module, respectively (Figures 1B and 1C; see Figure S2 and Table 1 for details). GCaMP2ΔRSET•Ca²⁺ has a compact structure with the M13 helix forming an intramolecular interaction with the CaM moiety (Figure 1C). The cpEGFP module in GCaMP2 and the isolated domain are very similar in structure to GFP-S65T (rmsd of 0.48 and 0.22 Å, respectively). To further assess the folded state and conformation of the cpEGFP module in GCaMP2 and in isolation in an unbiased way, distance difference analyses based on corresponding Cα positions were performed (Figure 1D; see Supplemental Experimental Procedures). The comparison of cpEGFP (lower part of the matrix) and GCaMP2ΔRSET (upper half of the matrix) with the structure of GFP-S65T (Ormo et al., 1996) produced featureless matrices indicating that cpEGFP is properly folded in both structures, indistinguishable in ternary structure to intact GFP (blue: distances showing minimal difference between two structures). Minor conformational changes were restricted to a single loop (residues 66–72 in GCaMP2, corresponding to residues 154–160 in GFP) and the N-terminal three residues of the first β sheet of the C-EGFP (Figure 1) that connect to the M13 fragment (residues 62–64 in GCaMP2/cpEGFP) (Figure 1). The latter region contributed to an intact β-barrel in cpEGFP, but is peeled away when the M13 helix is bound to the CaM domain in GCaMP2ΔRSET•Ca²⁺, producing a hole in the cpEGFP cage (Figures 1B–1D; see below). Based on these results, we can rule out major conformational changes in the cpEGFP module as the basis of Ca²⁺ sensitivity of GCaMP2.

Fluorophore Coordination in GCaMP2 and cpEGFP

Structural and spectroscopic studies have identified hallmarks of the distinct states of GFP manifested in the coordination of the fluorophore (Brejc et al., 1997; Yang et al., 1996). In the proton-

ated state characterized by a major absorbance peak at 395 nm, hydrogen bonds between Glu-222, Ser-205, and the fluorophore contribute to the neutralization of its phenolic oxygen. In the state with an absorbance maximum at 489 nm (e.g., GFP-S65T or EGFP), an anionic phenolate is stabilized by interactions with Thr-203 and His-148 of the β-barrel (Brejc et al., 1997; Ormo et al., 1996) (Figure 2A, bottom).

The interaction between the fluorophore and the threonine residue is preserved in the structure of Ca²⁺-bound GCaMP2ΔRSET (Thr-116 in GCaMP2ΔRSET; Figure 2A, top). Additional hydrogen bonds with two water molecules complete the sp³ hybridization of the phenolic oxygen, indicative of an ionic, bright fluorophore. In contrast, the structure of cpEGFP resembles features of a protonated fluorophore, as evidenced by the loss of a hydrogen bond between Thr-116 and the phenolic oxygen of the fluorophore, and the presence of a hydrogen bond between Glu-135 and Ser-118 (Glu-222 and Ser-205 in GFP-S65T) (Figure 2A, middle). The fluorophore itself and other residues involved in coordination and maturation of the fluorophore (residues Gln-252 and Arg-254 in GCaMP2; residues 94 and 96 in GFP-S65T) adopt very similar conformations in all the structures (Figure S3A) (Ormo et al., 1996).

The structural analysis is consistent with emission and excitation properties of the proteins. GCaMP2ΔRSET behaves similarly to the parent protein GCaMP2. In the absence of Ca²⁺, its fluorescence intensity is low with an absorbance maximum at 399 nm, indicative of a neutral fluorophore (Figure 2B). Upon Ca²⁺ binding, the absorbance maximum shifts to 488 nm, approximately a 5-fold increase at this wavelength compared with the apo-state, accompanied by a 7.5-fold increase in fluorescence intensity measured at 507 nm (Figure 2B). The absolute increase in fluorescence is slightly higher than the one reported previously for GCaMP2 (Hendel et al., 2008; Tallini et al., 2006), possibly due to the usage of a homogeneously monomeric sample (see below). In contrast, cpEGFP displays Ca²⁺-independent absorbance and emission properties and resided in a constitutively protonated

Table 1. Data Collection and Refinement Statistics

	cpEGFP	GCaMP2 Δ RSET Ca ²⁺ -Bound	GCaMP2 Dimer Ca ²⁺ -Bound (1)	GCaMP2 Dimer Ca ²⁺ -Bound (2)
Data Collection ^{a,b}				
Space group	P2 ₁ 2 ₁ 2 ₁	P4 ₁ 2 ₁ 2	C2	C2
Cell dimensions				
<i>a</i> , <i>b</i> , <i>c</i> (Å)	51.1, 62.2, 69.5	122.0, 122.0, 97.8	127.9, 47.3, 69.6	127.5, 47.0, 67.9
α , β , γ (°)	90.0, 90.0, 90.0	90.0, 90.0, 90.0	90.0, 100.7, 90.0	90.0, 100.9, 90.0
Resolution (Å)	50–1.45 (1.50–1.45)	50–2.00 (2.07–2.00)	50–1.75 (1.81–1.75)	50–2.60 (2.69–2.60)
<i>R</i> _{sym}	4.2 (13.2)	12.7 (71.0)	4.0 (21.1)	14.2 (44.1)
<i>I</i> / <i>σ</i> <i>I</i>	43.3 (9.9)	23.6 (3.7)	35.5 (5.0)	8.0 (2.3)
Completeness (%)	99.3 (93.2)	100.0 (100.0)	100.0 (99.9)	98.0 (85.5)
Measured reflections	302,513	881,335	188,674	41,030
Unique reflections	39,659	50,531	41,444	12,458
Redundancy	7.6 (4.1)	17.4 (15.2)	4.6 (4.3)	3.3 (2.6)
Refinement ^c				
Resolution (Å)	50–1.45	50–2.00	50–1.75	50–2.60
<i>R</i> _{work} / <i>R</i> _{free} ^d	13.2/17.5	16.3/18.7	16.8/21.4	22.4/27.0
Free R test set size (#/%)	3171/8.1	4821/10.0	4076/10.1	1167/10.1
No. atoms				
Protein	1851	3194	3158	3054
Ligand/ion	—	4 (Ca ²⁺)	4 (Ca ²⁺)	4 (Ca ²⁺)
Water	383	453	518	55
<i>B</i> -factors				
Protein	13.40	28.19	23.95	28.91
Ligand/ion	n.a.	28.93	16.29	44.65
Water	34.70	34.11	38.78	24.18
rmsd				
Bond lengths (Å)	0.011	0.008	0.019	0.003
Bond angles (°)	1.510	1.126	1.664	0.739

^aValues as defined in SCALEPACK (Otwinowski and Minor, 1997).^bHighest resolution shell is shown in parenthesis.^cValues as defined in PHENIX (Adams et al., 2002). All structures were solved by molecular replacement.^dNo sigma cutoffs.

state with an absorbance maximum at 399 nm and low fluorescence intensity (Tsien, 1998) (Figure 2C). Consistent with its high fluorescence and deprotonated fluorophore observed in the crystal structure, EGFP absorbed maximally at a peak wavelength of 488 nm both in the presence and absence of Ca²⁺ (Figure 2D). These results suggest that the Ca²⁺-dependent change in fluorescence derives from the fact that the destabilized fluorophore in cpEGFP is protonated at physiological pH, and that Ca²⁺ binding to calmodulin, and the attendant interaction with the M13 peptide, restores the deprotonated fluorophore structure, resulting in a marked increase in GFP fluorescence.

Direct Contacts between cpEGFP and CaM Determine the Bright State of GCaMP2

We next examined the molecular basis for the fluorophore stabilization described above. The Ca²⁺-bound CaM module has a tight grip on the M13 helix, bringing the CaM and cpEGFP moieties into close proximity with a buried surface area of 1581 Å² (4287 Å² including M13) at the interface (Figure 3A). It is interest-

ing to note that the CaM domain forms a ring-shaped seal around a hole in the cpEGFP cage that is present due to the circular permutation and partially exposes the fluorophore to solvent (Figure 3A), a positioning that would enable protection of the exposed residues.

The interaction between CaM and cpEGFP is facilitated by a concentration of positively charged residues at the surface of cpEGFP that can form favorable contacts with an overall negatively charged CaM domain (Figure 3B). In addition, there is a considerable amount of shape complementarity in the interfacial region (Figure 3A) that allows a continuous hydrogen bond network to form along the β -barrel of cpEGFP and the point of permutation (Figure 3C). Central to the interface along the vertical axis of the cpEGFP cage are two arginine residues, Arg-81 in cpEGFP and Arg-377 in CaM. Notably, Arg-377 forms a weak hydrogen bond with the carbonyl main-chain group of Thr-116 (Thr-203 in GFP-S65T), a residue involved in stabilizing the fluorophore in the ionized state (see above). His-148 in GFP-S65T, another residue involved in fluorophore coordination in the bright state, is missing in GCaMP2. Instead, Arg-377 forms

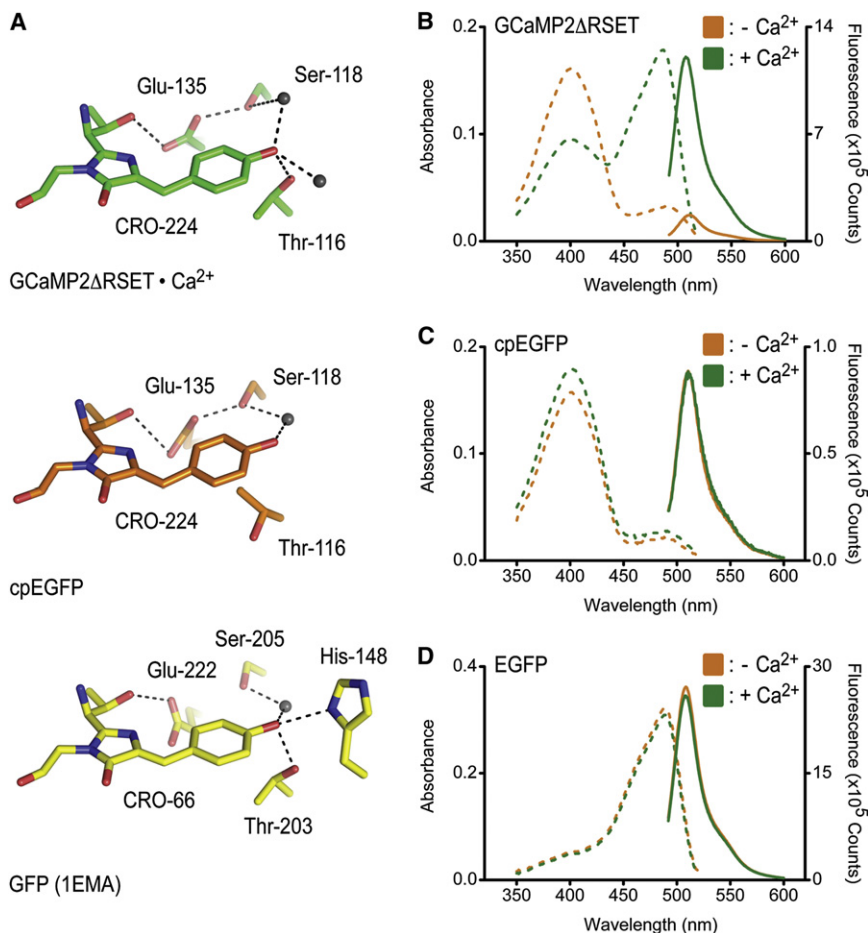


Figure 2. Coordination of the Fluorophore in Structures of GCaMP2 and cpEGFP

(A) Close-up view of the fluorophore-interacting residues in GCaMP2ΔRSET•Ca²⁺ (top), cpEGFP (middle), and GFP-S65T (bottom). Residue labeling is according to GCaMP2 numbering, except labeling of residues in the structure of GFP-S65T (PDB code 1EMA) (Ormo et al., 1996). Hydrogen bonds are shown as dashed lines.

(B) Spectroscopic properties of GCaMP2ΔRSET. Absorbance (dashed lines) and fluorescence emission (solid lines) spectra were measured at 25°C in Ca²⁺-free (10 mM EGTA; orange) buffer or in the presence of Ca²⁺ (40 μM; green). See [Experimental Procedures](#) for experimental details.

(C) Spectroscopic properties of cpEGFP. Experimental conditions were identical to (B).

(D) Spectroscopic properties of EGFP. Experimental conditions were identical to (B).

a water-mediated interaction with the fluorophore, suggesting that Arg-377 is functionally equivalent to His-148 (Figures 3C and 3D).

Significant design efforts yielded an optimized linker sequence connecting the functional moieties of GCaMP2 (Nakai et al., 2001). Most of these regions were resolved in the crystal structure of GCaMP2•Ca²⁺ (except for a 15-residue fragment connecting the two parts of EGFP). Linkers were found to be peripherally involved in the packing of the domains and as such might restrict interdomain flexibility. From the multitude of interactions at the interface, Arg-81 appears to be a central coordinator (Figures 3C and 3D). It is hydrogen-bonded to Glu-61 (and Glu-387), one of the two residues linking the M13 fragment to cpEGFP (Figures 1A and 3C). In addition, it is indirectly linked to Arg-304 located in the linker connecting the cpEGFP and CaM moieties (via Thr-382; Figure 3C). The linker length appears to be important as well (Nakai et al., 2001), constraining the conformational freedom of the system even further (see below).

Mutating Arg-377, Arg-81, or its binding partner Glu-387 (to alanine) resulted in a diminished fluorescence signal upon Ca²⁺ binding but did not affect the emission intensity in the absence of Ca²⁺ (Figure 4A), whereas equivalent mutations of Arg-81 in cpEGFP and EGFP affected the fluorescence intensity only slightly (Figures 4B and 4C). A double-mutant Arg-81-Ala/Glu-387-Ala, removing both side chains of the interacting resi-

dues, showed only moderate effects on Ca²⁺-dependent fluorescence increase compared with the single mutation, consistent with either modification disrupting the bright state conformation. In contrast, the double-mutant Arg-81-Ala/Arg-377-Ala exhibited markedly reduced Ca²⁺ sensitivity indicative of additive contributions of Arg-81 and Arg-377 to the interdomain interface and overall mechanism. Mutating the linker residue Glu-61 to either glycine or lysine generated a defective probe with intermediate fluorescence intensity but lacking Ca²⁺ responsiveness (Figure 4A). Therefore, the negative charge of Glu-61 appears to stabilize the neutral state of the fluorophore under Ca²⁺-free conditions, reducing its background fluorescence. Taken together, the mutagenesis data suggest that contributions from several residues collectively account for the performance of GCaMP2.

Consistent with a shift in fluorophore protonization as the general mechanism of Ca²⁺-dependent fluorescence, the interactions between cpEGFP and CaM described above contributed to an increase in apparent acidity of the fluorophore in Ca²⁺-bound GCaMP2ΔRSET (Figure S3B) (Nakai et al., 2001). The apparent pK_a value for the high-fluorescent state was 6.9, ~0.8 units lower than under Ca²⁺-free conditions, which is consistent with data reported for GCaMP1 (Nakai et al., 2001). In contrast, cpEGFP was less sensitive to pH, with pK_a values of 7.4 in the absence of Ca²⁺ and 7.9 in the presence of Ca²⁺. These values were approximately 1.5 units higher than the one determined for EGFP (Patterson et al., 1997) (Figure S3C), further confirming that increased solvent accessibility due to circular permutation is the major determinant for the neutral low-fluorescent state (Baird et al., 1999).

Taken together, Ca²⁺ sensing by GCaMP2 can be described as a switching from a class 1 to a class 2 GFP by restricting solvent access of the fluorophore and stabilizing it in an ionized form (Tsien, 1998).

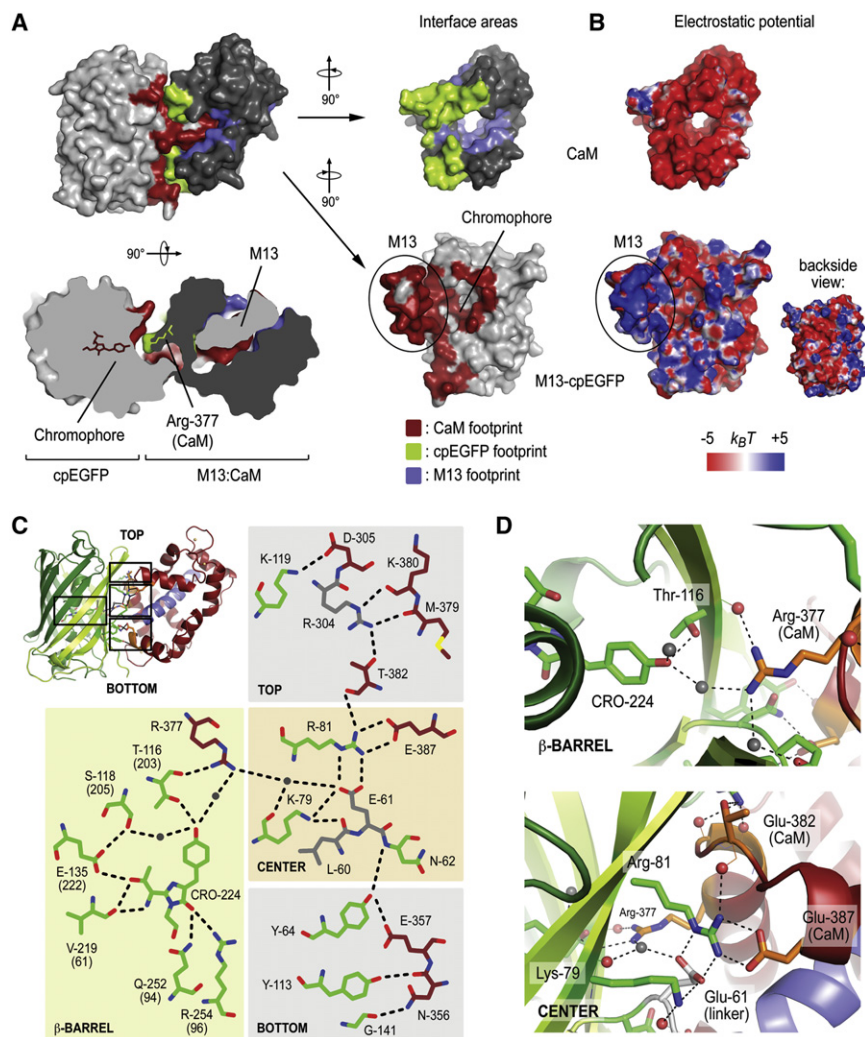


Figure 3. Intramolecular Interfaces in Monomeric GCaMP2•Ca²⁺

(A) Interfaces among the cpEGFP, M13, and CaM modules in the structure of monomeric GCaMP2 Δ RSET•Ca²⁺. Residues of the M13-cpEGFP module interacting with CaM are colored red. Interfacial residues on CaM are colored in green and blue for contacts with cpEGFP and the M13 helix, respectively. A top view, rotated 90° around the horizontal axis with respect to the view shown above, is shown as a cutaway rendition of the surface (bottom-left). The fluorophores of cpEGFP and Arg-377 of CaM are shown in stick presentation. Surface presentation of the isolated CaM domain and M13-cpEGFP unit were rotated by +90° and -90°, respectively, with respect to the view of the assembled structure (top-left). (B) Electrostatic potential of the M13-cpEGFP module and CaM mapped onto its molecular surface. Views are identical to (A). Red represents negative and blue represents positive potential (-5 to +5 $k_B T$).

(C) Schematic diagram of the fluorophore environment and the hydrogen bond network between cpEGFP and CaM. The numbering scheme for GCaMP2 was used. Corresponding residue numbers in GFP are shown in brackets. Carbon atoms of residues in cpEGFP, CaM, and linker segments are shown in green, dark red, and gray, respectively. Hydrogen bonds shown in the figure are between 2.7 and 3.3 Å (not drawn to scale).

(D) Close-up views of the interfacial regions in GCaMP2 Δ RSET•Ca²⁺. Water-mediated interaction between the fluorophore and Arg-377 of the CaM domain (top) and cpEGFP:CaM interfacial residues (bottom) are shown.

Structural Characterization of the Ca²⁺-Bound and Ca²⁺-free State of GCaMP2 in Solution

Analysis of GCaMP2 by size exclusion chromatography (SEC) suggested that Ca²⁺-bound GCaMP2 adopted a conformation similar but not identical to the Ca²⁺-free state (Figure 5A), with the Ca²⁺-bound state being slightly more compact based on its retention time. To further explore the conformational changes occurring upon Ca²⁺ binding, we carried out small angle X-ray scattering (SAXS) experiments, yielding molecular geometry parameters such as the radius of gyration (R_g) and maximum diameter of a molecule or assembly (D_{max}) (Table 2). The scattering profiles for the Ca²⁺-free and Ca²⁺-bound state were very similar at low angles (corresponding to the range of momentum transfer of $0.019 < S < 0.13 \text{ \AA}^{-1}$) (Figure 5B). Radii of gyration and maximum diameters of the two states calculated from the scattering profiles were comparable ($R_g[+\text{Ca}^{2+}] = 23.1 \pm 0.5$ versus $R_g[-\text{Ca}^{2+}] = 23.7 \pm 0.5$; $D_{max}[+\text{Ca}^{2+}] = 70.0 \pm 2.0$ versus $D_{max}[-\text{Ca}^{2+}] = 68.0 \pm 2.0$), indicating an overall similar shape. Distance distribution functions $[P(r)]$ corroborated this finding but also revealed a conformational change between GCaMP2 in the presence or absence of Ca²⁺. In the Ca²⁺-free state, the peak of the $P(r)$ function shifted about 5 Å toward larger dimension com-

pared with the $P(r)$ function for GCaMP2•Ca²⁺ or the corresponding profile calculated from the coordinates of the crystal structure (Figure 5C). This apparent compaction of GCaMP2 upon Ca²⁺ binding is consistent with the gel filtration experiments (see above).

To investigate the origin of these differences, we calculated low-resolution ab initio shape reconstructions (see Experimental Procedures) (Figures 5D and 5E). Envelopes (shown in gray) represent the overall shape of GCaMP2 at a maximum resolution of $\sim 30 \text{ \AA}$. The shape reconstruction of the Ca²⁺-bound state agreed very well with the crystal structure obtained for GCaMP2 Δ RSET•Ca²⁺ (Figure 5D). In contrast, Ca²⁺-free GCaMP2 adopted a donut-shaped conformation with a central hole in the center of the envelopes. Although one side of the envelope could accommodate the structure of cpEGFP, the other side had dimensions that fit the structure of Ca²⁺-free apo-CaM very well (Babu et al., 1988) (Figure 5E).

The overall similar dimensions of Ca²⁺-free and Ca²⁺-bound GCaMP2 and the shape reconstructions suggest that apo-GCaMP2 exists in a predocked state, likely to be stabilized by electrostatic interactions and the short nature of the linker segments connecting the domains in GCaMP2 (see above). Such

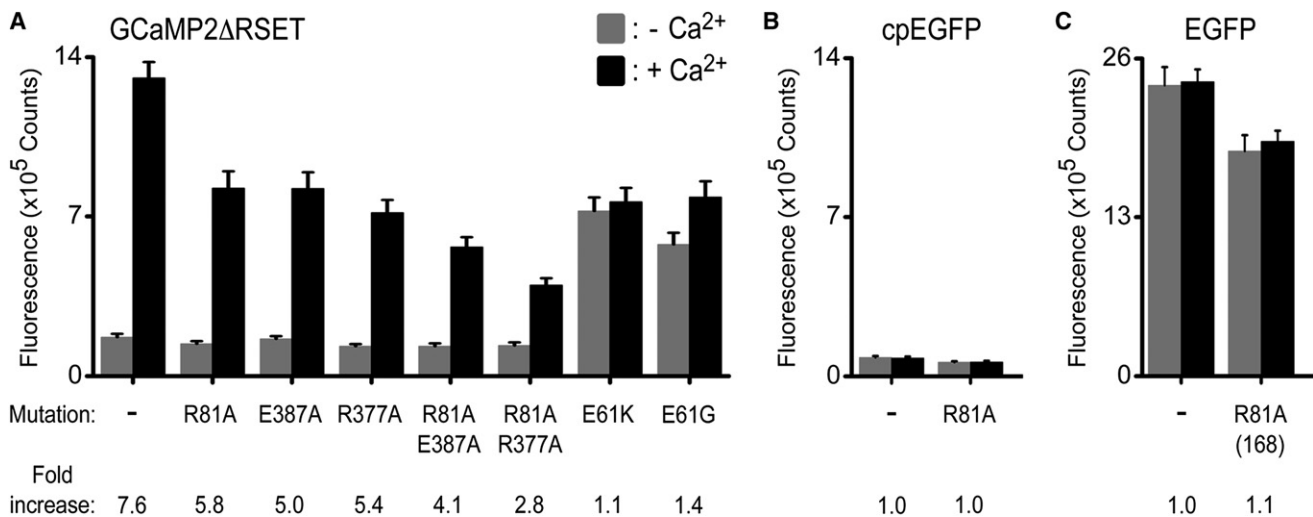


Figure 4. Mutational Analysis of GCaMP2•Ca²⁺

(A) Mutations in GCaMP2ΔRSET. Interfacial residues shown in Figures 3C and 3D were mutated. The fluorescence emission spectra were recorded in the presence (black) and absence (gray) of Ca²⁺. Bar diagrams show emission at 507 nm.

(B) Fluorescence emission of corresponding mutations in the isolated cpEGFP module.

(C) Fluorescence emission of corresponding mutations in EGFP. The GCaMP2 numbering scheme was used. Arg-81 is equivalent to Arg-168 in GFP and EGFP.

a conformation might explain the rapid kinetics of Ca²⁺-induced changes in GCaMP2 that happen on a millisecond timescale (Nakai et al., 2001; Tallini et al., 2006).

Identification of a Dimeric, Low-Fluorescent State of GCaMP2•Ca²⁺

During the purification of the proteins from *Escherichia coli*, we noticed a bimodal distribution of GCaMP2 and GCaMP2ΔRSET in SEC (Figures 6A and 6B). Analysis by analytical ultracentrifugation revealed that GCaMP2 coexisted in a monomeric and a dimeric state (Figure 6A), with the monomer peak eluting at 15.3 ml and the dimer peak, accounting for about 55% of the sample, eluting at 13.7 ml from a size exclusion column (Figure 6B). The dimer was sensitive to treatment with ethylene glycol tetraacetic acid (EGTA) (Figure 6B). The EGTA-treated protein eluted with a slightly shorter retention time than the monomer peak of the input protein, indicating that both the dimeric and monomeric species purified from bacterial lysates were bound to Ca²⁺ (Figure 6B). Absorbance and emission profiles of the Ca²⁺-bound monomer-dimer mixture indicated a half-maximal efficiency with regard to fluorescence intensity compared with the EGTA-treated, monomeric protein (Figures 6C and 2B). The partial response could be attributed to the monomeric fraction in the sample that accounted for 45% of the sample (Figures 6A–6C). The spectroscopic analysis suggested that the dimeric state of GCaMP2 is a Ca²⁺-bound, low-fluorescence state.

The results were consistent with structural studies on the basis of crystal structures of the Ca²⁺-bound dimeric state (Figure 6D). Crystals were obtained in two independent trials (Figure S4A), starting from a partially dimeric protein (Figure 6A) or from a sample that was purified in a monomeric state (Figure 4A). In solution, the latter protein remained monomeric upon Ca²⁺ addition suggesting that the high protein concentration and crystallization condition contributed to dimer formation. The structure showed

a domain-swapped assembly, in which the M13 helix of one molecule was bound to the CaM moiety of a crystal symmetry-related molecule (Figure 6D). Comparison of the dimeric and monomeric states showed that the M13 helices and CaM domains were separated by a rotation of about 26° and 90°, respectively, relative to cpEGFP. The CaM domain of a symmetry-related molecule in the dimer occupied the approximate position of CaM in the monomeric structure (Figures 6D and 6E). However, interfacial areas in the dimer were overall less extensive and overlapped only partially with areas that were buried in the monomeric, Ca²⁺-bound conformation (Figures S4B and S4C, Figure 3A). Most notably, interactions between cpEGFP and CaM did not occlude the hole in the β-barrel cage introduced by circular permutation, leaving the fluorophore solvent-exposed in such a conformation (Figure S4B and S4C).

The fluorophore environment in the dimeric structure reflected the spectroscopic properties discussed above. The phenolic oxygen of the fluorophore formed hydrogen bonds with two water molecules. Thr-116 (Thr-203 in GFP-S65T) adopted a rotamer conformation incompetent of chromophore stabilization, characteristic of a low-fluorescent, protonated state also observed in the structure of cpEGFP (Figure 6F). The structural studies corroborated the notion, based on the spectroscopic analysis, that the dimeric state of GCaMP2 is Ca²⁺-insensitive.

Conclusions

Here, we described the molecular mechanism underlying Ca²⁺-dependent fluorescence of the high-signal, genetically encoded Ca²⁺ sensor GCaMP2 based on high-resolution crystal structures and solution scattering studies. Many aspects of the particular design of GCaMP2 are likely to contribute to the success of this Ca²⁺ indicator, including the particular point of permutation allowing for reversible solvent exposure of the fluorophore, the complementarity between interfaces, and the functional

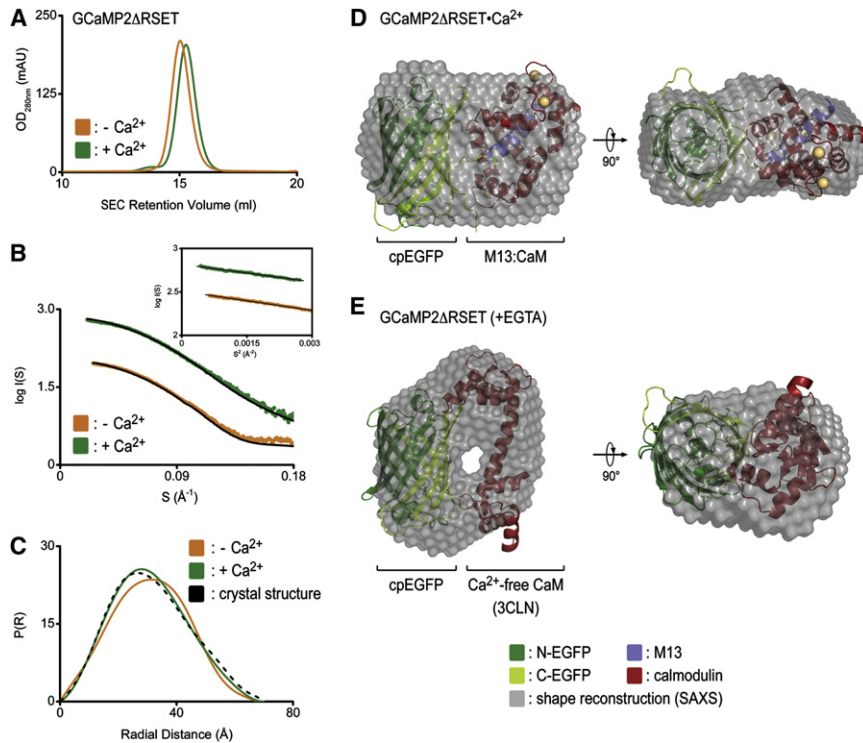


Figure 5. SAXS-Based Shape Reconstruction of GCaMP2 in the Presence or Absence of Ca^{2+}

(A) Size exclusion chromatographic analysis of GCaMP2 in the presence and absence of Ca^{2+} . GCaMP2ΔRSET was purified in its monomeric state (see [Experimental Procedures](#) for details). Proteins were analyzed on a S200 gel filtration column (10/300; GE Healthcare) in gel filtration buffer containing EGTA (10 mM; orange trace) or Ca^{2+} (1 mM; green trace). (B) Solution scattering data for GCaMP2ΔRSET in its Ca^{2+} -bound and Ca^{2+} -free state. Small-angle X-ray scattering curves of GCaMP2ΔRSET• Ca^{2+} (green) and its EGTA-treated form (orange) are shown after averaging and solvent subtraction. Theoretical scattering profiles calculated from the ab initio models with the lowest χ values are shown (black line). The inset shows Guinier plots (including linear fits) at the low-angle region ($S_{\text{max}} \cdot R_g < 1.3$). (C) Distance distribution $[P(r)]$ functions for GCaMP2ΔRSET. $P(r)$ curves of GCaMP2ΔRSET• Ca^{2+} (green) and its EGTA-treated form (orange) were calculated from SAXS data shown in (B) or from the crystal structure of GCaMP2ΔRSET• Ca^{2+} (dashed line). (D) SAXS-based shape reconstruction of GCaMP2ΔRSET• Ca^{2+} . The overall volume from shape reconstructions after averaging (gray envelope) was calculated from 40 independent models.

The crystal structure of monomeric GCaMP2ΔRSET• Ca^{2+} was docked into the envelope manually. Two orthogonal views are shown.

(E) SAXS-based shape reconstruction of Ca^{2+} -free GCaMP2ΔRSET. Details are as described in (C). The crystal structures of cpEGFP and Ca^{2+} -free CaM (PDB code 3CLN) (Babu et al., 1988) were docked into the envelope manually.

conservation of fluorophore-coordinating residues. Our results indicate that circular permutation of EGFP destabilizes the deprotonated state of the fluorophore, and that this state is re-established in a Ca^{2+} -dependent manner through intensive con-

tacts between the condensed CaM:M13 structure and EGFP moieties. A predocked state of CaM in the absence of Ca^{2+} might contribute to the rapid transition between the two fluorophore states.

Table 2. SAXS Data Statistics

	R_g (Å) ^a	D_{max} (Å) ^b	MM_{seq} (kDa) ^c	MM_{exp} (kDa) ^d	V_p (nm ³) ^e	$I_p^{\text{norm}}/I_{\text{std}}^{\text{norm}}$ ^f	NSD ^g
10 mM EGTA	23.7 ± 0.5	68.0 ± 2.0	50.7	45.9 ± 5	79 ± 8	0.91 ± 0.10	0.63 ± 0.02
40 μM Ca^{2+}	23.1 ± 0.5	70.0 ± 2.0	50.7	46.2 ± 5	66 ± 7	0.92 ± 0.10	0.54 ± 0.01

^a R_g determined from Guinier equation and data that satisfies $Q_{\text{max}} \cdot R_g < 1.3$; similar values were obtained using the program GNOM (Svergun, 1992).

^b D_{max} was determined using the program GNOM (Svergun, 1992).

^c MM_{seq} is the molecular mass calculated from the primary sequence.

^d MM_{exp} is the molecular mass calculated from the scattering data:

$$MM_{\text{protein}} = MM_{\text{lysozyme}} \times \frac{I_p^{\text{protein}} \times C_{\text{lysozyme}}}{I_p^{\text{lysozyme}} \times C_{\text{protein}}}$$

where MM_{lysozyme} is the molecular mass of lysozyme, I^0 is the scattering intensity and C (mg/ml) is the protein concentration (Petoukhov and Svergun, 2006).

^e V_p is the excluded volume (Porod volume) calculated using PRIMUS (Konarev et al., 2003; Petoukhov and Svergun, 2006; Porod, 1982).

^f Normalized intensities for proteins (p) I_p^{norm} were calculated by

$$I_p^{\text{norm}} = \left(\frac{I_p^0}{C} \right) / MM_{\text{seq}}$$

where I^0 is the intensity calculated using the Guinier equation and C (mg/ml) is the protein concentration determined from its absorbance at 280 nm. Lysozyme served as a monodispersed protein standard (std). Ideally, the ratio $I_p^{\text{norm}}/I_{\text{std}}^{\text{norm}}$ equals 1.00 (Jeffries et al., 2008; Taraban et al., 2008).

^g After superimposing the independently modeled envelopes, pairwise normalized spatial discrepancy (NSD) values (Volkov and Svergun, 2003) were calculated as part of the DAMAVER routine. NSD values close to unity indicate good agreement between individual models.

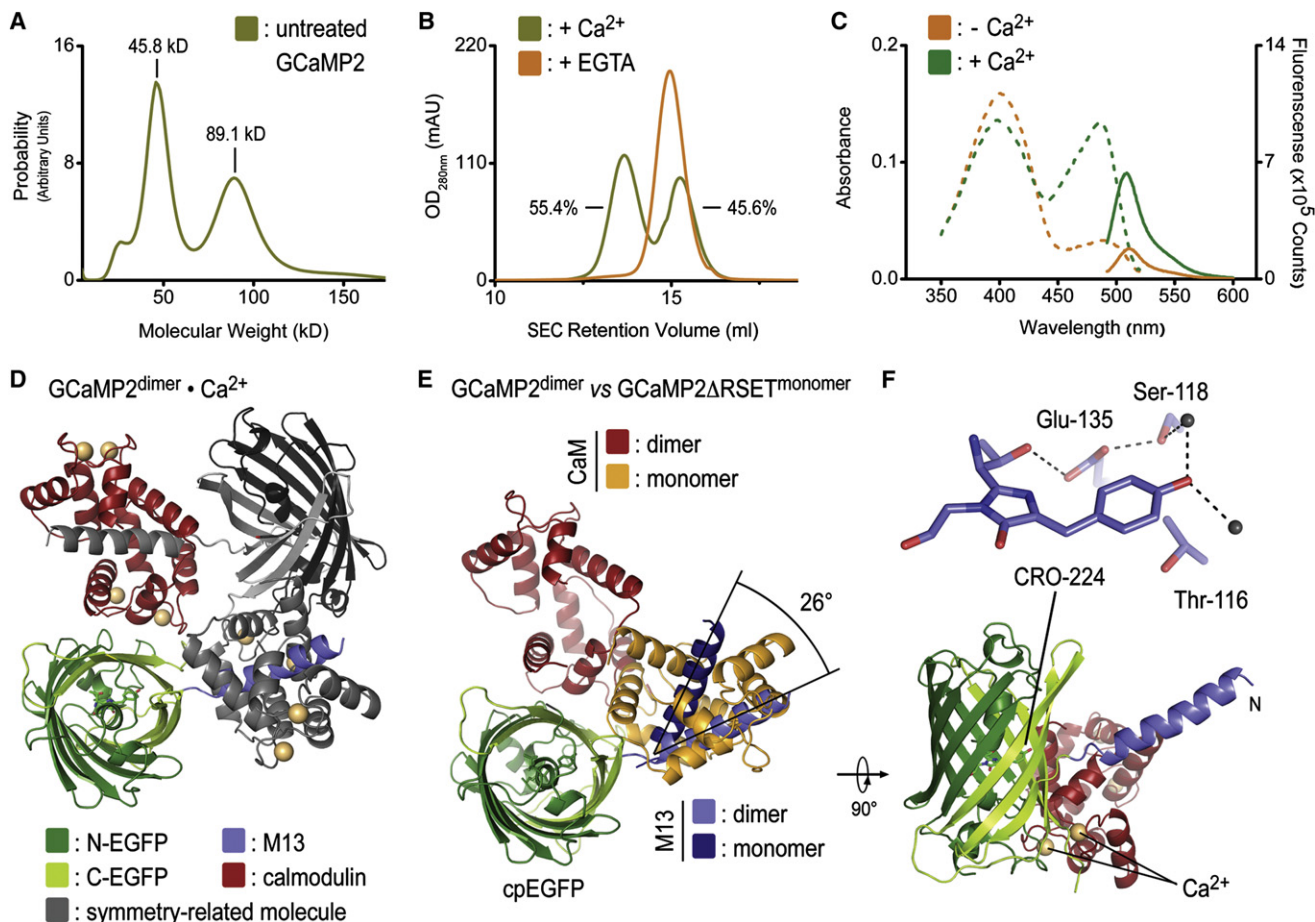


Figure 6. Characterization and Crystal Structure of Dimeric GCaMP2 $\bullet\text{Ca}^{2+}$

(A) Identification of a dimeric GCaMP2 by analytical ultracentrifugation. Sedimentation velocity experiments using GCaMP2 purified from *E. coli* yielded bimodal molecular weight distributions with masses (45.8 kDa and 89.1 kDa) close to the theoretical mass of monomeric (50.7 kDa) and dimeric GCaMP2 (101.4 kDa), respectively.

(B) Monomerization of GCaMP2 by EGTA-treatment. Size exclusion chromatograms for initial preparation of GCaMP2 showed bimodal distribution of the protein. Both peaks were sensitive to EGTA treatment, converging to a single peak corresponding to Ca^{2+} -free, monomeric protein. EGTA treatment produced protein that remained monomeric in the presence or absence of Ca^{2+} (see Figure 5A).

(C) Spectroscopic properties of partially dimeric GCaMP2. Absorbance (dashed lines) and fluorescence emission (solid lines) spectra were measured at 25°C in Ca^{2+} -free (10 mM EGTA; orange) buffer or in the presence of Ca^{2+} (40 μM ; green).

(D) Crystal structure of the dimeric assembly. Crystals were grown from partially dimeric Ca^{2+} -bound GCaMP2. A crystallographic dimer of GCaMP2 is shown with protomer colored according to the scheme introduced in Figure 1A, and a crystal symmetry-related molecule shown in gray. Ca^{2+} is shown as yellow spheres.

(E) Superposition of monomeric and dimeric GCaMP2. A single protomer of dimeric GCaMP2, colored as in (D), was superimposed on the cpEGFP domain of monomeric GCaMP2 $\Delta\text{RSET}\bullet\text{Ca}^{2+}$, with its M13 helix and CaM module colored in dark blue and orange, respectively.

(F) Fluorophore coordination in dimeric GCaMP2 $\bullet\text{Ca}^{2+}$. A close-up view of the fluorophore-interacting residues in dimeric GCaMP2 $\bullet\text{Ca}^{2+}$ is shown. Residue labeling is according to GCaMP2 numbering.

The complex and extensive nature of the interactions underlying this mechanism carries important implications for the design of GECIs and other molecular sensors based on the cpEGFP platform. First, achieving the reversible destabilization of a bright state with other fluorescent proteins or fusion peptides by random means will likely require extensive mutagenesis and screening, as occurred with the development of GCaMP2. Forward design of structures to achieve this goal would seem more likely to yield effective signaling molecules. Second, the surface properties such as charge and shape complementarity of the fluorescent module and the fusion peptides should be considered so

as to optimize the kinetics of state transition and minimize interactions with other binding partners. Alternatively, the incorporation of binding sites (e.g., a CaM binding site) could also confer a predocked state. However, the results might suggest that it is unlikely that marked improvement in kinetics will be achieved using current cpEGFP-based signaling proteins. Although this might limit the utility of these GECIs for the most rapid cell signaling events (Hendel et al., 2008; Mao et al., 2008; Tallini et al., 2006), GCaMP2 transitions occur in less than 100 ms at physiological temperatures, which is sufficient for many signaling processes. Third, the discovery of a dimeric dim state indicates

the importance of preventing intermolecular binding, because these proteins contribute to background fluorescence and thereby could markedly limit the dynamic range of the signaling system. In summary, our studies provide a structural basis for future improvements in the rational design of protein-based signaling molecules and identify key limitations to this strategy.

EXPERIMENTAL PROCEDURES

Protein Expression and Purification

The coding regions corresponding to GCaMP2, EGFP, and cpEGFP were amplified by standard PCR and were cloned into the pRSET expression plasmid (Nakai et al., 2001). GCaMP2ΔRSET was cloned into a modified pET28a expression plasmid (Novagen) yielding N-terminally hexahistidine-tagged SUMO fusion proteins. The hexahistidine-tagged SUMO-moiety was cleavable using the protease from Ulp-1 from *Saccharomyces cerevisiae*.

Transformed *E. coli* cells BL21(DE3) (Novagen) were grown in TB medium supplemented with 50 mg/l antibiotics at 37°C. At a cell density corresponding to an absorbance of 1.0 at 600 nm the temperature was reduced to 18°C, and protein production was induced with 1 mM IPTG. Proteins were expressed for 12–16 hrs. Cells were collected by centrifugation, resuspended in NINTA buffer A (25 mM Tris-Cl [pH 8.2], 500 mM NaCl and 20 mM imidazole). After cell lysis by sonication, cell debris was removed by centrifugation at 40,000 g for 1 hr at 4°C. Clear lysates were loaded onto HisTrap NINTA columns (GE Healthcare) equilibrated in NINTA buffer A. The resin was washed with 20 column volumes NINTA buffer A, and proteins were eluted in a single step with NINTA buffer A supplemented with 500 mM imidazole. GCaMP2ΔRSET was incubated with SUMO protease ULP-1 at 4°C overnight for removal of the hexahistidine-SUMO tag, and the cleaved protein was collected in the flow-through during NINTA affinity chromatography. Proteins were further subjected to size exclusion chromatography on a Superdex200 column (16/60; GE Healthcare) equilibrated in gel filtration buffer (100 mM NaCl, 25 mM HEPES [pH 7.4]).

Ca²⁺-free proteins were produced by incubation in gel filtration buffer supplemented with 10 mM EGTA before the size exclusion column. Fractions containing protein were pooled and concentrated on a Centricon ultrafiltration device (10 kDa cutoff; Millipore). Protein aliquots were frozen in liquid nitrogen and stored at –80°C.

Point mutations were generated using the QuikChange XL Mutagenesis Kit (Stratagene) following the manufacturer's instructions. Expression and purification of mutant proteins was identical to the procedure described for parent proteins. Mutant proteins showed size exclusion profiles in the presence or absence of Ca²⁺ indistinguishable from original proteins.

Analytical size exclusion chromatography was carried out on a Superdex200 column (10/300; GE Healthcare) equilibrated in gel filtration buffer at a protein concentration of 0.2 mM (initial concentration). EGTA ("–Ca²⁺"); 10 mM) or CaCl₂ (1 mM) was present where indicated.

Crystallization, X-Ray Data Collection, and Structure Solution

Crystals were obtained by hanging drop vapor diffusion by mixing equal volumes of protein (~10–30 mg/ml) and reservoir solution at 20°C (if not indicated otherwise). For cpEGFP, the reservoir solution comprised 0.1 M Tris (pH 8.5) and 2.4 M diammonium hydrogen phosphate. Crystals for monomeric GCaMP2ΔRSET•Ca²⁺ grew in 20% PEG8000, 0.1 M HEPES (pH 7.5), 1.6 M ammonium sulfate, and 1 mM CaCl₂ at 4°C. The reservoir solution for crystallization of dimeric GCaMP2•Ca²⁺ consisted of 0.2 M sodium formate, 20% PEG 3350, 10 mM MgCl₂, and 1 mM CaCl₂ (dimer 1), or 0.2 M MgCl₂, 0.1 M Bis-Tris (pH 6.5), 25% PEG3350, and 1 mM CaCl₂ (dimer 2). During preparation of this article a third crystallization condition has been reported, producing crystals within the same space group and similar unit cell constants (Rodríguez Guilbe et al., 2008). Crystals producing the structure of dimer 1 were grown from partially dimeric protein (as judged by size exclusion chromatography and analytical ultracentrifugation). The structure of dimer 2 was obtained from EGTA-treated, monomeric protein. All crystals were cryoprotected using crystallization solutions supplemented with 20% xylitol, frozen in liquid nitrogen, and kept at 100 K during data collection.

Crystallographic statistics for data collection are shown in Table 1. Data sets were collected using synchrotron radiation at the Cornell High Energy Syn-

chrotron Source (CHESS; Ithaca, NY; beamline A1, wavelength 0.977Å). Data reduction was carried out with the software package HKL2000 (Otwinowski and Minor, 1997). Phases were obtained from molecular replacement using the software package PHENIX (Adams et al., 2002) with structures of GFP-S65T (Protein Data Base [PDB] code 1EMA) (Ormo et al., 1996) and Ca²⁺-bound calmodulin (PDB code 1MXE) (Clapperton et al., 2002) as search models. Manual refinement in COOT (Emsley and Cowtan, 2004) and minimization using PHENIX (Adams et al., 2002) yielded the final models with good geometry (with all residues being in allowed regions of the respective Ramachandran plots). Illustrations were made in Pymol (DeLano Scientific). Buried surface areas were calculated using the program CNS (Brunger et al., 1998). Electrostatic potentials were calculated using the program APBS (Baker et al., 2001).

SAXS and SAXS-Based Shape Reconstruction

The SAXS data were collected at CHESS (beamline G1) at an electron energy of 8KeV covering the range of momentum transfer 0.019 < S < 0.22 Å^{–1}. Buffer exchange into Ca²⁺-free (gel filtration buffer supplemented with 10 mM EGTA) and Ca²⁺-saturated (gel filtration buffer supplemented with 1 mM CaCl₂) buffer was carried out by SEC. Protein samples and buffer controls were centrifuged at 13,200 g for 20 min before data acquisition. Scattering data were collected in triplicates at protein concentrations between 5 and 20 mg/ml with exposure times of 5 s. Buffer background scattering was collected from gel filtration buffers used during buffer exchange. Background-subtraction, averaging, and scaling were carried out using the program PRIMUS (Konarev et al., 2003), and data were analyzed using the programs GNOM and CRY SOL (Svergun et al., 1995; Svergun, 1992). Only scattering data with S_{max}•R_g < 1.3, computed from Guinier plots at low-angle regions, were considered for further analysis. Kratky plots, experimental molecular weight determinations, and normalized scattering intensities were used to assess the folded state of the proteins and overall data quality using the program IGOR PRO (version 5.04B). Distance distribution functions P(r) and D_{max} were determined using the program GNOM (Svergun, 1992).

Ab initio free atom modeling was performed using the program DAMMIN (Svergun, 1999) with the scattering curve as the fitting target. Forty independent simulations are carried out for each protein. Superposition, averaging, and filtering using the program DAMAVER (Volkov and Svergun, 2003) yielded shape reconstructions. Calculated scattering curves and goodness of fit (χ) were calculated using the program CRY SOL (Svergun et al., 1995).

Analytical Ultracentrifugation

Sedimentation velocity experiments were carried out using an XL-I analytical ultracentrifuge (Beckman Coulter) equipped with an AN-60 Ti rotor. Proteins (5–15 μM) were diluted in AUC buffer (100 mM NaCl, 25 mM HEPES [pH 7.4], and 1 mM TCEP) and were analyzed at a centrifugation speed of 40,000 rpm. Data collection was carried out at 280 nm, followed by data analysis using the program SedFit (version 11.0) using default parameters.

Absorbance and Fluorescence Spectroscopy

Absorbance spectra (320–500 nm; 10 mm path length) of purified proteins (20 μM) were recorded in duplicate on a DU730 UV/Vis spectrophotometer (Beckman Coulter) at 25°C. Emission spectra (495–600 nm) were recorded in triplicate on a fluorescence spectrophotometer (Photon Technology International) at a protein concentration of 100 nM and an excitation wavelength of 488 nm. The Ca²⁺ calibration buffer kit (Biotium, Inc) was used to create accurate assay conditions with regard to Ca²⁺ concentration. Ca²⁺ sensitivity of purified proteins was determined by measuring the fluorescence intensity at 508 nm under Ca²⁺-free (10 mM EGTA) and Ca²⁺-saturated conditions (40 μM Ca²⁺). Sensitivity to changes in pH was measured at a protein concentration of 10 μM using buffers containing sodium acetate (pH 4.5–5.0), MES (pH 5–6.5), HEPES (pH 6.5–8), or CHES (pH 8.5–10). pK_a values were calculated by fitting the experimental data to the Hill equation.

ACCESSION NUMBERS

Atomic coordinates and structure factors have been deposited in the RCSB Protein Data Bank under the ID codes 3EVP, 3EVR, 3EVU, and 3EVV.

SUPPLEMENTAL DATA

Supplemental Data include Supplemental Experimental Procedures and four figures and can be found with this article online at [http://www.cell.com/structure/supplemental/S0969-2126\(08\)-004139](http://www.cell.com/structure/supplemental/S0969-2126(08)-004139).

ACKNOWLEDGMENTS

We are grateful to the scientists and staff members at CHESS for assistance with synchrotron data collection, and to the scientist at the protein facility at Cornell for assistance with analytical ultracentrifugation experiments. We thank Gary Peng for his assistance with plasmid preparation and Lei Tan (Rockefeller University) for her contribution of MATLAB code used in the distance matrix analysis. This work was supported by grants HL45239, DK65992, and EB006782 from the National Institutes of Health (M.I.K.).

Received: August 21, 2008

Revised: August 21, 2008

Accepted: October 11, 2008

Published: December 9, 2008

REFERENCES

- Adams, P.D., Grosse-Kunstleve, R.W., Hung, L.W., Ioerger, T.R., McCoy, A.J., Moriarty, N.W., Read, R.J., Sacchettini, J.C., Sauter, N.K., and Terwilliger, T.C. (2002). PHENIX: building new software for automated crystallographic structure determination. *Acta Crystallogr. D Biol. Crystallogr.* **58**, 1948–1954.
- Babu, Y.S., Bugg, C.E., and Cook, W.J. (1988). Structure of calmodulin refined at 2.2 Å resolution. *J. Mol. Biol.* **204**, 191–204.
- Baird, G.S., Zacharias, D.A., and Tsien, R.Y. (1999). Circular permutation and receptor insertion within green fluorescent proteins. *Proc. Natl. Acad. Sci. USA* **96**, 11241–11246.
- Baker, N.A., Sept, D., Joseph, S., Holst, M.J., and McCammon, J.A. (2001). Electrostatics of nanosystems: application to microtubules and the ribosome. *Proc. Natl. Acad. Sci. USA* **98**, 10037–10041.
- Brejck, K., Sixma, T.K., Kitts, P.A., Kain, S.R., Tsien, R.Y., Ormo, M., and Remington, S.J. (1997). Structural basis for dual excitation and photoisomerization of the Aequorea victoria green fluorescent protein. *Proc. Natl. Acad. Sci. USA* **94**, 2306–2311.
- Brunger, A.T., Adams, P.D., Clore, G.M., DeLano, W.L., Gros, P., Grosse-Kunstleve, R.W., Jiang, J.S., Kuszewski, J., Nilges, M., Pannu, N.S., et al. (1998). Crystallography and NMR system: a new software suite for macromolecular structure determination. *Acta Crystallogr. D Biol. Crystallogr.* **54**, 905–921.
- Clapperton, J.A., Martin, S.R., Smerdon, S.J., Gamblin, S.J., and Bayley, P.M. (2002). Structure of the complex of calmodulin with the target sequence of calmodulin-dependent protein kinase I: studies of the kinase activation mechanism. *Biochemistry* **41**, 14669–14679.
- Emsley, P., and Cowtan, K. (2004). Coot: model-building tools for molecular graphics. *Acta Crystallogr. D Biol. Crystallogr.* **60**, 2126–2132.
- Hendel, T., Mank, M., Schnell, B., Griesbeck, O., Borst, A., and Reiff, D.F. (2008). Fluorescence changes of genetic calcium indicators and OGB-1 correlated with neural activity and calcium in vivo and in vitro. *J. Neurosci.* **28**, 7399–7411.
- Jeffries, C.M., Whitten, A.E., Harris, S.P., and Trehwella, J. (2008). Small-angle X-ray scattering reveals the N-terminal domain organization of cardiac myosin binding protein C. *J. Mol. Biol.* **377**, 1186–1199.
- Konarev, P.V., Volkov, V.V., Sokolova, A.V., Koch, M.H.J., and Svergun, D.I. (2003). PRIMUS: a Windows PC-based system for small-angle scattering data analysis. *J. Appl. Crystallogr.* **36**, 1277–1282.
- Kotlikoff, M.I. (2007). Genetically encoded Ca²⁺ indicators: using genetics and molecular design to understand complex physiology. *J. Physiol.* **578**, 55–67.
- Ledoux, J., Taylor, M.S., Bonev, A.D., Hannah, R.M., Solodushko, V., Shui, B., Tallini, Y., Kotlikoff, M.I., and Nelson, M.T. (2008). Functional architecture of inositol 1,4,5-trisphosphate signaling in restricted spaces of myoendothelial projections. *Proc. Natl. Acad. Sci. USA* **105**, 9627–9632.
- Mank, M., and Griesbeck, O. (2008). Genetically encoded calcium indicators. *Chem. Rev.* **108**, 1550–1564.
- Mao, T., O'Connor, D.H., Scheuss, V., Nakai, J., and Svoboda, K. (2008). Characterization and subcellular targeting of GCaMP-type genetically-encoded calcium indicators. *PLoS ONE* **3**, e1796.
- Miyawaki, A., Llopis, J., Heim, R., McCaffery, J.M., Adams, J.A., Ikura, M., and Tsien, R.Y. (1997). Fluorescent indicators for Ca²⁺ based on green fluorescent proteins and calmodulin. *Nature* **388**, 882–887.
- Miyawaki, A., Griesbeck, O., Heim, R., and Tsien, R.Y. (1999). Dynamic and quantitative Ca²⁺ measurements using improved cameleons. *Proc. Natl. Acad. Sci. USA* **96**, 2135–2140.
- Nagai, T., Sawano, A., Park, E.S., and Miyawaki, A. (2001). Circularly permuted green fluorescent proteins engineered to sense Ca²⁺. *Proc. Natl. Acad. Sci. USA* **98**, 3197–3202.
- Nagai, T., Yamada, S., Tominaga, T., Ichikawa, M., and Miyawaki, A. (2004). Expanded dynamic range of fluorescent indicators for Ca(2+) by circularly permuted yellow fluorescent proteins. *Proc. Natl. Acad. Sci. USA* **101**, 10554–10559.
- Nakai, J., Ohkura, M., and Imoto, K. (2001). A high signal-to-noise Ca(2+) probe composed of a single green fluorescent protein. *Nat. Biotechnol.* **19**, 137–141.
- Nausch, L.W., Ledoux, J., Bonev, A.D., Nelson, M.T., and Dostmann, W.R. (2008). Differential patterning of cGMP in vascular smooth muscle cells revealed by single GFP-linked biosensors. *Proc. Natl. Acad. Sci. USA* **105**, 365–370.
- Ormo, M., Cubitt, A.B., Kallio, K., Gross, L.A., Tsien, R.Y., and Remington, S.J. (1996). Crystal structure of the Aequorea victoria green fluorescent protein. *Science* **273**, 1392–1395.
- Otwinowski, Z., and Minor, W. (1997). Processing of X-ray diffraction data collected in oscillation mode. In *Methods in Enzymology*, C.W. Carter, Jr. and R.M. Sweet, eds. (New York: Academic Press), pp. 307–326.
- Palmer, A.E., and Tsien, R.Y. (2006). Measuring calcium signaling using genetically targetable fluorescent indicators. *Nat. Protoc.* **1**, 1057–1065.
- Patterson, G.H., Knobel, S.M., Sharif, W.D., Kain, S.R., and Piston, D.W. (1997). Use of the green fluorescent protein and its mutants in quantitative fluorescence microscopy. *Biophys. J.* **73**, 2782–2790.
- Petoukhov, M.V., and Svergun, D.I. (2006). Joint use of small-angle X-ray and neutron scattering to study biological macromolecules in solution. *Eur. Biophys. J.* **35**, 567–576.
- Pologruto, T.A., Yasuda, R., and Svoboda, K. (2004). Monitoring neural activity and [Ca²⁺] with genetically encoded Ca²⁺ indicators. *J. Neurosci.* **24**, 9572–9579.
- Porod, G. (1982). General theory. In *Small-Angle X-Ray Scattering*, O. Kratky, ed. (London: Academic Press), pp. 17–51.
- Reiff, D.F., Ihring, A., Guerrero, G., Isacoff, E.Y., Joesch, M., Nakai, J., and Borst, A. (2005). In vivo performance of genetically encoded indicators of neural activity in flies. *J. Neurosci.* **25**, 4766–4778.
- Rodriguez Guilbe, M.M., Alfaro Malave, E.C., Akerboom, J., Marvin, J.S., Loder, L.L., and Schreier, E.R. (2008). Crystallization and preliminary X-ray characterization of the genetically encoded fluorescent calcium indicator protein GCaMP2. *Acta Crystallogr. Sect. F Struct. Biol. Cryst. Commun.* **64**, 629–631.
- Roell, W., Lewalter, T., Sasse, P., Tallini, Y.N., Choi, B.R., Breitbach, M., Doran, R., Becher, U.M., Hwang, S.M., Bostani, T., et al. (2007). Engraftment of connexin 43-expressing cells prevents post-infarct arrhythmia. *Nature* **450**, 819–824.
- Souslova, E.A., Belousov, V.V., Lock, J.G., Stromblad, S., Kasparov, S., Bolshakov, A.P., Pinielis, V.G., Labas, Y.A., Lukyanov, S., Mayr, L.M., and Chudakov, D.M. (2007). Single fluorescent protein-based Ca²⁺ sensors with increased dynamic range. *BMC Biotechnol.* **7**, 37.

- Svergun, D., Barberato, C., and Koch, M.H.J. (1995). CRY SOL: a program to evaluate x-ray solution scattering of biological macromolecules from atomic coordinates. *J. Appl. Crystallogr.* 28, 768–773.
- Svergun, D.I. (1992). Determination of the regularization parameter in indirect-transform methods using perceptual criteria. *J. Appl. Crystallogr.* 25, 495–503.
- Svergun, D.I. (1999). Restoring low resolution structure of biological macromolecules from solution scattering using simulated annealing. *Biophys. J.* 76, 2879–2886.
- Tallini, Y.N., Ohkura, M., Choi, B.R., Ji, G., Imoto, K., Doran, R., Lee, J., Plan, P., Wilson, J., Xin, H.B., et al. (2006). Imaging cellular signals in the heart in vivo: cardiac expression of the high-signal Ca^{2+} indicator GCaMP2. *Proc. Natl. Acad. Sci. USA* 103, 4753–4758.
- Tallini, Y.N., Brekke, J.F., Shui, B., Doran, R., Hwang, S.M., Nakai, J., Salama, G., Segal, S.S., and Kotlikoff, M.I. (2007). Propagated endothelial Ca^{2+} waves and arteriolar dilation in vivo: measurements in Cx40BAC GCaMP2 transgenic mice. *Circ. Res.* 101, 1300–1309.
- Taraban, M., Zhan, H., Whitten, A.E., Langley, D.B., Matthews, K.S., Swint-Kruse, L., and Trewthella, J. (2008). Ligand-induced conformational changes and conformational dynamics in the solution structure of the lactose repressor protein. *J. Mol. Biol.* 376, 466–481.
- Tsien, R.Y. (1998). The green fluorescent protein. *Annu. Rev. Biochem.* 67, 509–544.
- Volkov, V.V., and Svergun, D.I. (2003). Uniqueness of ab initio shape determination in small-angle scattering. *J. Appl. Crystallogr.* 36, 860–864.
- Yang, F., Moss, L.G., and Phillips, G.N., Jr. (1996). The molecular structure of green fluorescent protein. *Nat. Biotechnol.* 14, 1246–1251.